Scalable Growth of Transition Metal Dichalcogenides for Next-Generation Nanoelectronics

S. W. Tong[a] and Man-Fai Ng[b]

[a] Institute of Materials Research and Engineering, Agency for Science, Technology and Research, 2 Fusionopolis Way, #08-03 Innovis, Singapore 138634
[b] Institute of High Performance Computing, Agency for Science, Technology and Research, 1 Fusionopolis Way, #16-16 Connexis, Singapore 138632

Atomically-thin semiconducting transitional metal dichalcogenides (TMDCs) are promising channel materials for future ultra-scaled electronic devices due to their high electron mobility attained at sub-nanometer thickness. In particular, monolayer WS_2 has shown the highest theoretical room temperature electron mobility among other semiconducting TMDCs as a result of its low effective mass. However, it is still challenging to grow large-area and strictly monolayer WS_2 through the conventional chemical vapor deposition (CVD) due to the uncontrollable growth kinetics. In this work, we provide a modified CVD process to prepare the uniform and large-area monolayer TMDCs. Theoretical simulations were performed to understand the fundamental thermodynamically mechanism of the monolayer growth. The property-variation in TMDCs due to difference in electronic structure between different layers of TMDCs can be significantly reduced based on this new approach. This poses a reliable route for the scalable growth of monolayer TMDCs, which is essential for their reliable applications in nanoelectronic devices.

Introduction

Alternative channel materials for future ultra-scaled electronic devices have been intensively pursued nowadays since the feature size of silicon-based transistors has been scaled down to their physical limit (1,2). Atomically-thin semiconducting transitional metal dichalcogenides (TMDCs) are promising channel materials for future ultra-scaled electronic devices because many two-dimensional TMDCs maintain good carrier transport even for atomically thin layers below 1 nm (2). In particular, monolayer WS_2 has shown the highest theoretical room temperature electron mobility among other semiconducting TMDCs as a result of its low effective mass (3). Combined with the large exciton/trion binding energy with high photoluminescence quantum yield, monolayer WS_2 is a strong candidate as a potential channel material for high-efficiency optoelectronic applications (4).

However, it is still challenging to grow highly uniform and strictly monolayer TMDCs continuous film through the conventional chemical vapor deposition (CVD) due to the uncontrollable growth kinetics. The evaporation rates and amounts of the heated precursors are uncontrollable because the saturation vapor pressure of the precursor is exponentially

dependent on the temperature inside the furnace. The sulfurized film is thus consisted of a mixture of monolayer, bilayer and multiple layers of TMDCs. The film with such unreproducible quality is not applicable for real industrial applications. To this end, we have recently employed a molybdate precursor with an in-situ alkali metal-based seed promotor to grow highly crystalline monolayer TMDCs crystals (edge length up to 260 μm) for high-performance field effect transistors with high electron mobility ~90 cm^2/Vs (5) and low contact resistance (6). In this work, we will demonstrate another growth approach based on the self-limiting CVD process to prepare the strictly monolayer and highly uniform TMDCs.

Experimental

Growth of monolayer WS_2 on 2-inch SiO_2/Si substrates

Before the CVD growth process, the SiO_2/Si substrates were firstly pre-deposited with 1.5 nm thick WO_3 film using sputtering method and then transferred into downstream zone (growth zone) of a two-zone vertical furnace. The pressure inside the furnace was then maintained at ~10 Torr, filled with constant flow rate of Ar:H_2 in a ratio of 3.5. The temperature of diethyl sulfide (DES, 98%, Sigma-Aldrich) was slowly increased to 30 °C to ensure stable sulfur supply from the bubbler. During the growth process, the DES source was pulse supplied by modulating its flow rate between 0 and 4 sccm with the mass flow controller under the constant temperature of 30 °C (Figure 1). Constant temperature of 600 °C was maintained in the upstream zone, while the temperature in the downstream zone was modulated within 600-950 °C. Thereafter, the sample was cooled naturally to room temperature under 200 sccm Ar gas flow.

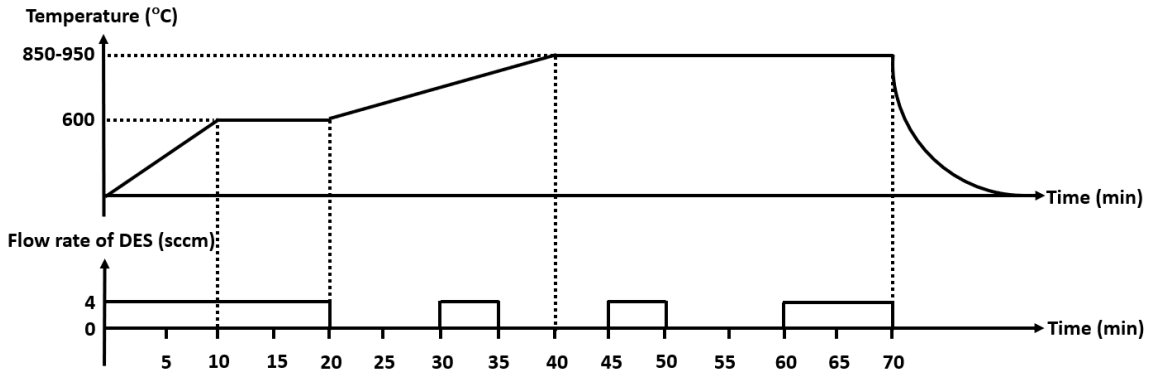

Figure 1. Heating profile of the downstream zone (upper graph) and flow rate of DES supply (lower graph) regulated inside the furnace throughout the growth process. The pulse supply of DES source is regulated by controlling the flow rate between 0 and 4 sccm.

Characterizations of WS_2

The morphological features and thickness of monolayer WS_2 were studied by using an optical microscope (Leica Microsystems, CH-9435) and Bruker Dimension FastScan Atomic Force Microscope (AFM) under the tapping mode. Micro-Raman and photoluminescence (PL) were performed by WITec alpha300S Raman imaging system with monochromatic laser source (λ of 532 nm) to identify the uniformity and thickness of WS_2. With a 100x objective lens (NA=0.9), 1800 and 600 gratings/mm were used for Raman and PL measurement respectively at room temperature. To determine the continuity of the synthesized WS_2, the freshly prepared WS_2 film was transferred from the growth substrate onto another SiO_2/Si substrate using the typical PMMA transfer technique (7).

Density functional theory (DFT) simulation

Geometry optimizations were performed using DFT within the generalized gradient approximation (GGA) in the form of Perdew, Burke, and Ernzerhof (PBE) exchange-correlation functional (8) implemented in Vienna Ab-initio Simulation Package (version 5.4) (9). The core−valence interaction was described by the projector augmented wave (PAW) method (10). The kinetic energy cutoff for the plane-wave expansion was set at 450 eV. The Gamma-centered sampling with a 5×5×1 k-point grid was used for the slab models. The ions and lattices were fully relaxed until the total energy and absolute value of the forces acting on each atom are less than 1×10^{-6} eV and 1×10^{-2} eV $Å^{-1}$, respectively. Dipole correction was applied. The vacuum was set at least 14 Å in order to minimize the spurious interactions between the neighboring images. The DFT-D3 method (11) was used to correct the dispersion interaction. For the WS_2 on SiO_2 model, (2x2) SiO_2 and (3x3) WS_2 are used. The lattice mismatch along the surface directions is less than 4.1 %. The thickness of the SiO_2 slab is about 10.9 Å. The bottom six layers (total thirteen layers) are frozen during optimizations.

Results and Discussions

Figure 2a shows the optical microscopic (OM) image of the as-grown WS_2 film grown on a 1'' SiO_2/Si. The homogeneous color contrast suggests that the full area coverage growth of WS_2 film on the substrate. The thickness and uniformity are further confirmed by a combination of Raman and Photoluminescence (PL) spectroscopy. Figure 2b shows two distinctive WS_2 Raman features located at ~356 cm^{-1} and ~418 cm^{-1} indicating the E_{2g} and A_{1g} vibrational modes respectively. The frequency difference of ~62 cm^{-1} between these two Raman peaks confirming that the WS_2 film is in monolayer thick with high crystallinity (12). The high-resolution mapping image based on Raman A_{1g} peak position in a 100 x 100 μm area (Figure 2c) serves as evidence of the high spatial continuity of WS_2 film. The film also displays the intense PL exciton peak located at 624 nm (13) with a narrow full width half maximum value of ~52 meV, which is also in agreement with the direct band gap nature of monolayer WS_2 (Figure 2d).

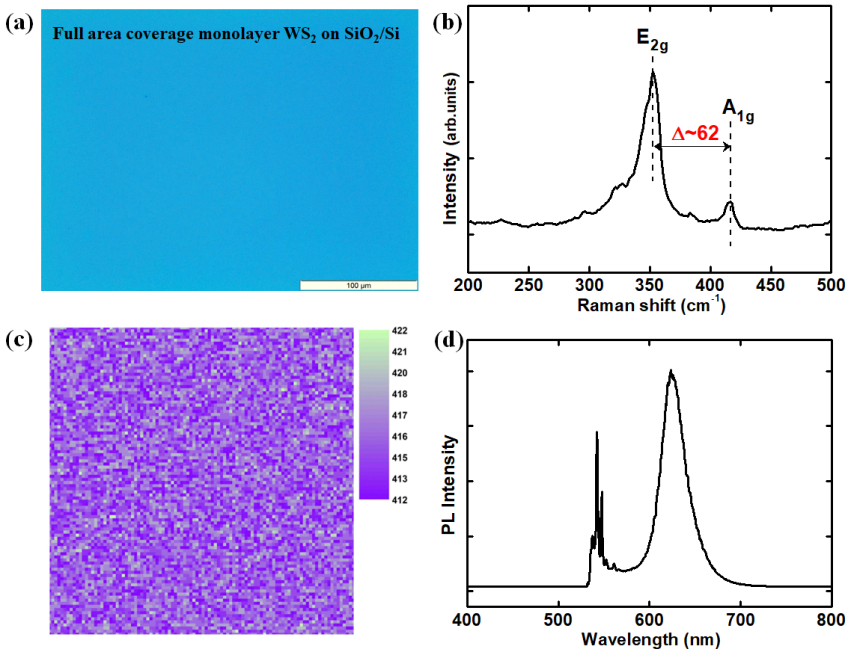

Figure 2. (a) Optical microscopic image of as-grown WS_2 film on SiO_2/Si. (b) Raman, (c) mapping image of Raman A_{1g} peak position (100 x 100 μm), and (d) PL of WS_2.

Having confirmed the monolayer nature, we next demonstrate the uniformity and small surface roughness of WS_2 film. Figure 3 shows the atomically smooth surface (root mean square roughness of 0.128 nm) of the as-grown WS_2 film based on atomic force microscopic study (AFM). The homogeneous surface can be verified from the negligible phase shift detected on the sample (Figure 3b), suggesting that our growth process could avoid overgrowth occur (i. e. inhibit the formation of multi-layered WS_2).

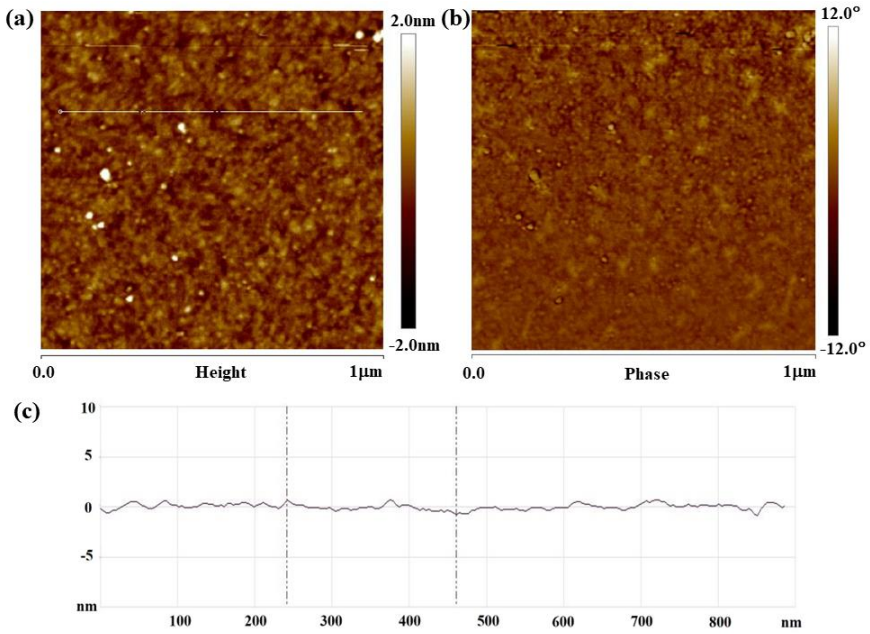

Figure 3. Tapping-mode AFM images of the as-grown WS_2 on SiO_2/Si. (a) Height image, (b) phase image, and (c) the cross-sectional profile extracted along the white line marked on the height image.

It is noted that monolayer WS_2 exhibits superior mechanical flexibility due to their atomically-thin structure and the ability to endure high mechanical strain. Therefore, as-grown WS_2 film can be transferred from the growth substrate onto another SiO_2/Si substrate using the typical PMMA transfer technique without damaging the film quality. AFM height image of the transferred WS_2 (Figure 4a) has confirmed that the continuity and uniformity can be maintained with only few defects were induced after the transfer process. The cross-sectional profile extracted along the blue line marked on the height image indicates that the thickness of WS_2 is around 0.8 nm (Figure 4b), confirming that our self-limiting grown monolayer WS_2 film can be facilely transferred. As shown in Figure 5, high Raman mode ratio of E_{2g}/A_{1g} can be retained, while the PL peak is slightly blue-shifted after the PMMA transfer process. Overall, the high quality of the sample is not affected after transfer with the release of tensile strain associated during growth.

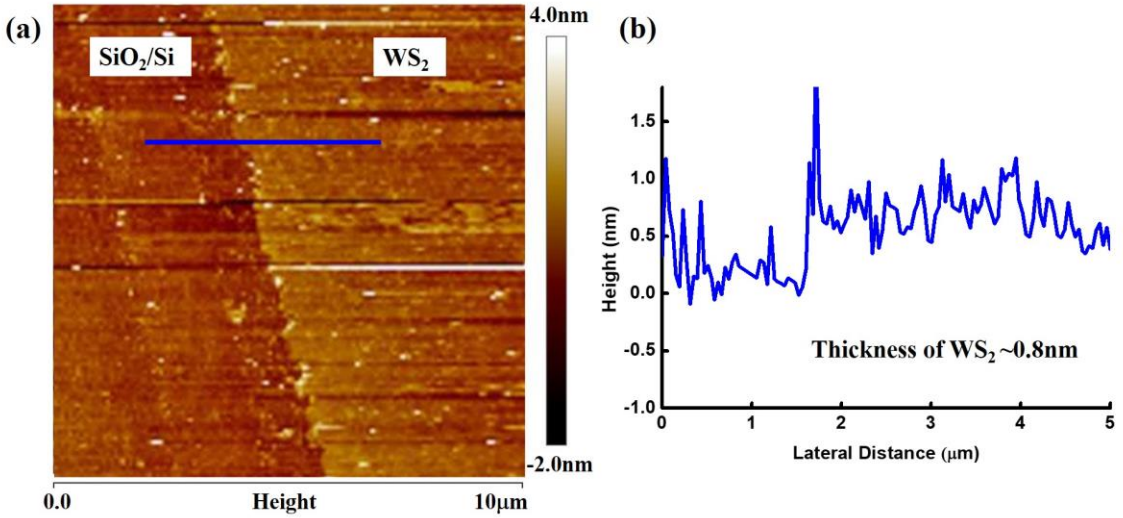

Figure 4. Tapping-mode AFM images of the transferred WS_2 on SiO_2/Si. (a) Height image and (b) the cross-sectional profile extracted along the blue line marked on the height image.

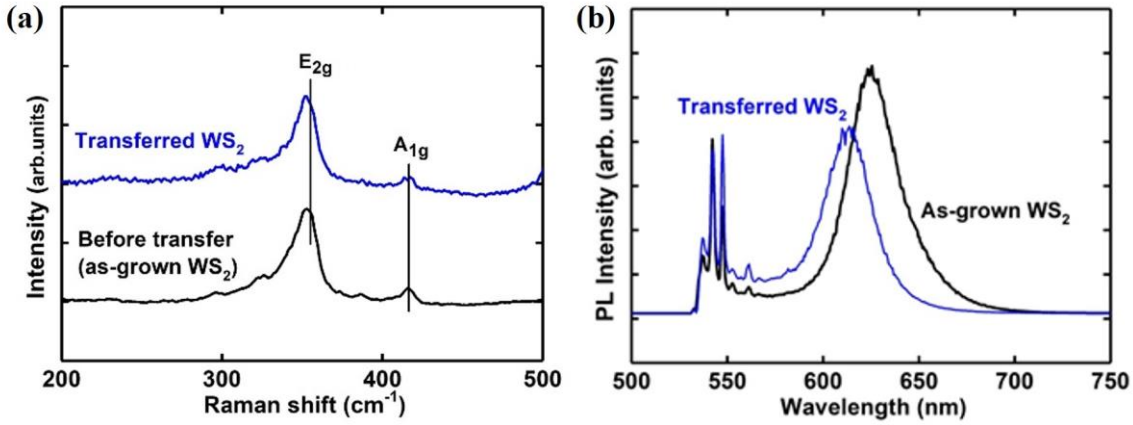

Figure 5. (a) Raman and (b) PL comparison between the as-grown WS_2 and transferred WS_2 films.

As the thermal stability of WS_2 is strongly dependent on the interface interaction, the binding energy (E_b) at the interface of WS_2-SiO_2 and WS_2-WS_2 is calculated by density functional theory (DFT) simulations (Figure 6) using the following equation:

$$E_b = E_{\mathrm{SiO2}+xWS_2} - (E_{\mathrm{SiO2}+(x-1)WS_2} + E_{WS_2})$$

where $E_{\mathrm{SiO2}+xWS_2}$, $E_{\mathrm{SiO2}+(x-1)WS_2}$ and E_{WS_2} are the total energies of the SiO_2 substrate plus x layer(s) of WS_2, the SiO_2 substrate plus $(x-1)$ layer of WS_2 (x equals either 1 or 2), and a monolayer WS_2, respectively. A more negative binding energy value was extracted from the WS_2- SiO_2 junction (-2.21 eV) as opposed to the one extracted from the WS_2-WS_2 interlayer (-1.94 eV) indicated that the monolayer WS_2 binds stronger on SiO_2, compared with the bilayers and multiple layers. Contrary to the more stable monolayer WS_2 on SiO_2 (with strong interface coupling), the instability of WS_2 overgrowth regions will be stripped off above a critical process temperature, together with the pulsed supply of DES supply in a continuous flow of Ar and H_2 gas environment.

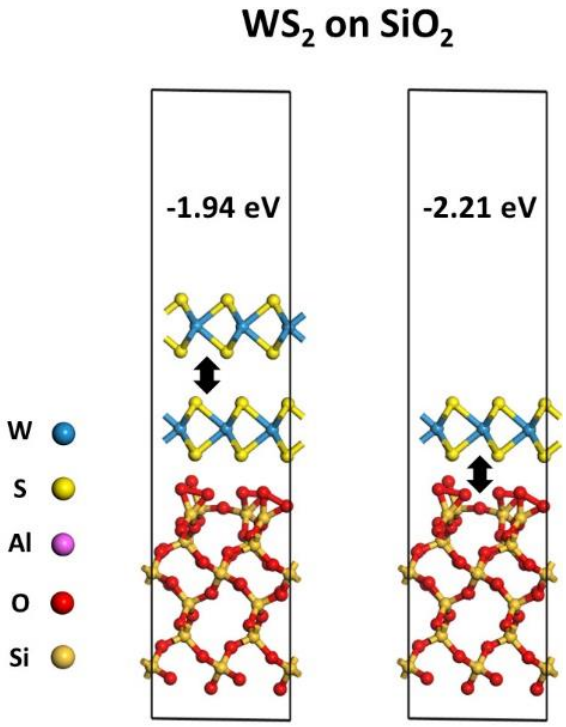

Figure 6. Slab models of bilayer (left) and monolayer (right) WS_2 on SiO_2.

Conclusions

The growth process of large-area monolayer WS_2 films displaying high photoluminescence and atomically smooth surface on amorphous SiO_2/Si substrate was demonstrated. This study shows that rational design in controlling the sulfur supply under the constant Ar/H_2 environment at a critical process temperature is a promising direction toward the reproducible growth of high-quality TMDC-based channel material for ultra-scaled nanoelectronics.

Acknowledgements

The authors gratefully acknowledge financial support from the Agency for Science, Technology, and Research (A*STAR) via A*STAR Science and Engineering Research Council (SERC Grant No SC25/21-803212).

References

1. D. Akinwande, C. Huyghebaert, C.-H. Wang, M. I. Serna, S. Goossens, L.-J. Li, H.-S. P. Wong, and F. H. L. Koppens, *Nature*, **573**, 507 (2019).
2. F. Wu, H. Tian, Y. Shen, Z. Hou, J. Ren, G. Gou, Y. Sun, Y. Yang, and T.-L. Ren, *Nature*, **603,** 259 (2022).
3. W. Zhang, Z. Huang, W. Zhang, and Y. Li, *Nano Res*., **7**, 1731 (2014).
4. Q. Wang, Q. Zhang, X. Luo, J. Wang, R. Zhu, Q. Liang, L. Zhang, J. Z. Yong, C. P. Y. Wong, G. Eda, J. H. Smet, and A. T. S. Wee, *ACS Appl. Mater. Interfaces*, 12, 45235 (2020).
5. S. W. Tong, H. Medina, W. Liao, J. Wu, W. Wu, J. Chai, M. Yang, A. Abutaha, S. Wang, C. Zhu, K. Hippalgaonkar, and D. Chi, *ACS Appl. Mater. Interfaces.,* **11**, 14239 (2019).
6. C. S. Lau, J. Y. Chee, Y. S. Ang, S. W. Tong, L. Cao, Z.-E. Ooi, T. Wang, L. K. Ang, Y. Wang, M. Chhowalla, and K. E. J. Goh, *ACS Nano* **14**, 13700 (2020).
7. Y.-F. Lim, K. Priyadarshi, F. Bussolotti, P. K. Gogoi, X. Cui, M. Yang, J. Pan, S. W. Tong, S. Wang, S. J. Pennycook, K. E. J. Goh, A. T. S. Wee, S. L. Wong, and D. Chi, *ACS Nano*, **12**, 1339 (2018).
8. J. P. Perdew, K. Burke, and M. Ernzerhof, *Phys. Rev. Lett.*, **77**, 3856 (1996).
9. G. Kresse and J. Furthmuller, *Phys. Rev. B*, **54**, 11169 (1996).
10. P. E. Blöchl, *Phys. Rev. B*, **50**, 17953 (1994).
11. S. Grimme, J. Antony, S. Ehrlich, and H. Krieg, *J. Chem. Phys*., **132**, 154104 (2010).
12. J. Chen, W. Zhou, W. Tang, B. Tian, X. Zhao, H. Xu, Y. Liu, D. Geng, S. J. R. Tan, W. Fu, and K. P. Loh, *Chem. Mater*. **28**, 7194 (2016).
13. P. Hu, J. Ye, X. He, K. Du, K. K. Zhang, X. Wang, Q. Xiong, Z. Liu, H. Jiang, and C. Kloc, *Sci. Rep*. **6**, 24105 (2016).